Biophysical Journal Volume 88 February 2005 1377–1386

Interpreting Second-Harmonic Generation Images of Collagen I Fibrils

Rebecca M. Williams, Warren R. Zipfel, and Watt W. Webb
Applied and Engineering Physics, Cornell University, Ithaca, New York 14853

ABSTRACT Fibrillar collagen, being highly noncentrosymmetric, possesses a tremendous nonlinear susceptibility. As a result, second-harmonic generation (SHG) microscopy of collagen produces extremely bright and robust signals, providing an invaluable tool for imaging tissue structure with submicron resolution. Here we discuss fundamental principles governing SHG phase matching with the tightly focusing optics used in microscopy. Their application to collagen imaging yields several biophysical features characteristic of native collagen structure: SHG radiates from the shell of a collagen fibril, rather than from its bulk. This SHG shell may correspond to the supporting element of the fibril. Physiologically relevant changes in solution ionic strength alter the ratio of forward-to-backward propagating SHG, implying a resulting change in the SHG shell thickness. Fibrillogenesis can be resolved in immature tissue by directly imaging backward-propagating SHG. Such findings are crucial to the design and development of forthcoming diagnostic and research tools.

INTRODUCTION

Multiphoton microscopy, based on nonlinear excitation of fluorescent probes, has become a standard method for noninvasive imaging of thick specimens with cellular resolution (Denk et al., 1990; Zipfel et al., 2003b). Coherent nonlinear microscopies, based on photon scattering, including second- or third-harmonic generation (SHG or THG) microscopy (Hellwarth and Christensen, 1974; Barad et al., 1997; Muller et al., 1998; Moreaux et al., 2000) or coherent anti-Stokes Raman scattering (CARS) microscopy (Volkmer et al., 2001; Cheng et al., 2002), can provide similar detailed sectioning at relatively benign energies. Of particular relevance to biological imaging are collagen, microtubules and myosin, all of which are tissue intrinsic and highly noncentrosymmetric molecular assemblies that possess first hyperpolarizabilities large enough for SHG microscopy (Freund and Deutsch, 1986; Williams et al., 2001; Campagnola et al., 2002; Dombeck et al., 2003; Zipfel et al., 2003a).

Fibrillar collagen is the most abundant protein in mammals and fortuitously an extremely bright second-harmonic generator, with a hyperpolarizability just 10-fold less than crystalline quartz (Fine and Hansen, 1971; Roth and Freund, 1979,1981; Freund et al., 1986). As a result, collagen SHG microscopy has recently become a robust tool for imaging tissue structure with cellular resolution, in both ex vivo and in vivo preparations (Guo et al., 1999; Williams et al., 2001; Campagnola et al., 2002; Stoller et al., 2002b; Wang et al., 2002; Brown et al., 2003; Zipfel et al., 2003a). Collagen SHG signal yields images of general tissue structure as well as boundaries (capsules or structural membranes) between tissue types. With such capabilities, it provides a potent tool for visualizing the pathological effects of disease on the extracellular matrix. For example, SHG microscopy has shown that in tumor models collagen adopts an abnormal structure on which transformed cells exhibit increased motility (Wang et al., 2002; Brown et al., 2003).

Because it is a coherent optical process, the principles underlying SHG microscopy are more complex than those of multiphoton fluorescence microscopy. Phase matching must be accounted for from all parts of the nonlinear focal volume (Moreaux et al., 2000; Mertz and Moreaux, 2001) based on its well-understood phase profile (Richards and Wolf, 1959). Because phase information is retained, nonlinear scattering microscopies enable opportunities for gleaning information from signal directionality in addition to signal intensity. Type I collagen fibrils are particularly interesting because they are thick, with diameters comparable to the wavelength of visible light (Parry et al., 1978; Craig and Parry, 1981).

Here we elucidate basic principles for interpreting SHG microscope images and demonstrate how these rules apply to analysis of tendon collagen (type I). We show that collagen SHG radiates from a hollow tube defined by the surface layers of the fibril. The effective thickness of this SHG shell is below the resolution limit for optical microscopy and strongly dependent on the ionic strength of the surrounding solution. High-resolution images from backward propagating SHG can be used to identify punctuate segmental collagen characteristic of ongoing fibrillogenesis in young tissues or collagen turnover in older tissues. Because SHG microscopy can be accomplished in vivo (Wang et al., 2002; Brown et al., 2003; Larson et al., 2003; Flesken-Nikitin et al., 2004), the technique exhibits promise for biomedical assessment of tissue structure, especially in processes where the extracellular matrix is being actively remodeled, such as in wound healing, malignancy, or development.

Submitted June 8, 2004, and accepted for publication October 26, 2004.

Address reprint requests to Rebecca M. Williams, 212 Clark Hall, Cornell University, Ithaca, NY 14853. Tel.: 607-255-8034; E-mail: rw36@cornell.edu.

0006-3495/05/02/1377/10 $2.00

doi: 10.1529/biophysj.104.047308

METHODS

SHG microscopy

Second-harmonic was generated using a Spectra Physics (Mountain View, CA) Ti:Sapphire laser (Millenium-Tsunami combination) providing ~100 fs pulses at 80 MHz at 700–1000-nm wavelengths. Beam scanning and image acquisition were performed with a BioRad Radiance 2000-MP scanning system (Hemel Hempstead, UK) interfaced with an Olympus IX70 (Melville, NY) inverted microscope. Linear illumination polarization with an adjustable orientation at the specimen was set using a Berek variable waveplate (5540, New Focus, San Jose, CA) placed before the scanner. The efficiency of collagen SHG increases as one tunes the fundamental to the shorter wavelength regions of the Ti:Sapphire tuning range (Zipfel et al., 2003a). Note, however, that for vital imaging, this <800-nm wavelength regime can be nonoptimal for several reasons. Illumination of live specimens with these wavelengths results in reduced cell viability (Williams et al., 1999), and the effective imaging depth lessens with the resulting shorter, more scattering SHG wavelengths (Zipfel et al., 2003a). Generally for these experiments the focusing objective consisted of a Zeiss 20 × 0.75 numerical aperture (N.A.) Fluar (Jena, Germany), the illumination wavelength was centered at 780 nm, and blocking of the fundamental was accomplished with BGG22 and 390/10 filters (Chroma Technology, Rockingham, VT). Unless specifically stated, the fundamental was adjusted to be parallel to the tendon axis, and the SHG intensity was detected without polarization selection. All exceptions to these general conditions are noted in the figure captions.

Backscattered SHG was collected in epi-mode with a dichroic (Chroma, 670DCXXRU) placed directly after the objective back aperture. SHG was separated into one of three photomultiplier tubes (PMTs) (R1924A-HA, Hamamatsu, Bridgewater, NJ) located in the microscope turret and the resulting signal amplified and sent to the external inputs of the Radiance. When necessary, SHG polarization separation was accomplished with a broadband polarizing cube beamsplitter (10FC16PB.3, Newport, Irvine, CA) and two polarizers (New Focus, 5511) placed within this unit.

Forward SHG was collected using a 40×, 0.8 N.A. water immersion Olympus LUMPlanFL objective and a bialkali PMT assembly (Hamamatsu, HC125-02). The forward collection objective was spatially positioned for maximal collection of a two-photon excited fluorescent standard. Forward SHG polarization analysis was performed by rotating an analyzer (New Focus, 5511) in between the specimen and the forward PMT assembly. To image the SHG propagation profile, the illumination beam was held stationary in the specimen and a Nikon D1H camera (Melville, NY) equipped with a macro lens was focused at the back aperture of the forward collecting objective, a setup designed to image the Fourier plane from a focused spot in the specimen.

SHG from tendon is extremely bright. High-quality images can easily be collected from intensities that have been shown to be safe for cells (a few mW through a high-N.A. lens; Williams et al., 1999). Tendon collagen is also extremely photostable and exhibits no signs of photodamage at powers as high as 50 mW with long laser dwell times (ms). However, with a beam that is stationary (for seconds to minutes) for spectroscopic measurements (Zipfel et al., 2003a) or SHG diffraction images, an artifactual photo-induced green fluorescence was sometimes observed to appear, especially with illumination wavelengths <750 nm. If necessary, the illumination power was reduced accordingly for a stable signal.

Tendon specimens

All results presented were obtained from fresh Sprague-Dawley rat tails, stored refrigerated for no longer than 24 h. (Tendons from frozen tails exhibited results similar to those shown for fresh fibrils; these results are not presented within this article.) Fibrillogenesis and age-dependent SHG data are acquired from littermates sacrificed at different ages. All other results are from adult specimens. To extract tendons, tails were cut into ~1-cm sections and the tendons slid out axially through the tendon sheathing. For the ionic experiments, the tendons were immersed directly in pure water buffered to pH 7.4 with 20 mM HEPES. The tendons were attached to the coverslip on both ends with wax so as to render them immobile upon introduction of solutions. Varying strength osmotic solutions prepared using small and large osmolites (sorbitol and 8000 MW polyethylene glycol), as controls, had no significant effects. The few tendons to be fixed were incubated in 3.8% paraformaldehyde for 1 h. For all other experiments, the tendons were placed in physiological saline and imaged within 3 h of extraction.

Note that adult tendons can be several hundred microns thick, so that an uncalibrated ratio of SHG collected by forward versus backward detectors is meaningless. F/B depends upon the image depth within the tendon, the tendon's absorption and scattering properties, and the relative collection efficiency of the two detectors. All F/B measurements are thus normalized to blue-emitting 5-μm fluorescent beads (A7305, Molecular Probes, Eugene, OR) infused within the tendon, whose forward/backward fluorescence ratio is assumed to be one.

Theory: SHG polarization from collagen fibrils

The polarization (electric dipole moment per unit volume) induced by an electric field **E** is given (in Gaussian units) by:

$$\mathbf{P} = \mathbf{P}_0 + \boldsymbol{\alpha} : \mathbf{E} + \boldsymbol{\beta} : \mathbf{EE} + \boldsymbol{\gamma} : \mathbf{EEE} + \ldots, \qquad (1)$$

where $\mathbf{P}_0$ is the static dipole density, $\boldsymbol{\alpha}$ is the polarizability matrix, and $\boldsymbol{\beta}$ and $\boldsymbol{\gamma}$ are the first- and second-order hyperpolarizability matrices. The $\boldsymbol{\alpha}$, $\boldsymbol{\beta}$, and $\boldsymbol{\gamma}$ nomenclature has been used traditionally as the molecular equivalent to the various order macroscopic susceptibilities $\boldsymbol{\chi}^{(n)}$. Note that the matrices in some sources vary by a scalar value according to whether the $1/n!$ term from the Taylor series expansion is included within the hyperpolarizabilities (Willetts et al., 1992).

By the definition in Eq. 1, an incident laser field at (x, y, z) with a frequency ω induces a second-order polarization at 2ω in the ith direction given by:

$$P_{2\omega,\mathrm{i}}(x,y,z) = \sum_{\mathrm{j,k}} \langle \beta_{\mathrm{ijk}}(x,y,z) \rangle E_{\omega,\mathrm{j}}(x,y,z) E_{\omega,\mathrm{k}}(x,y,z). \qquad (2)$$

Assuming both cylindrical and Kleinman symmetries (Freund et al., 1986; Boyd, 1992), the first-order hyperpolarizability matrix for a z-directed beam on a y-aligned fiber reduces to just two elements:

$$\begin{aligned} P_{2\omega,\mathrm{y}} &= \beta_{\mathrm{yyy}} E_{\omega,\mathrm{y}}^2 + \beta_{\mathrm{yxx}} E_{\omega,\mathrm{x}}^2 \\ P_{2\omega,\mathrm{x}} &= \beta_{\mathrm{yxx}} E_{\omega,\mathrm{x}} E_{\omega,\mathrm{y}}, \end{aligned} \qquad (3)$$

where $E_{\omega,\mathrm{x}}$ and $E_{\omega,\mathrm{y}}$ are the fundamental field strengths polarized in the x and y directions, respectively. Note that for linearly polarized light being focused with an N.A. < 0.8 objective, the polarization is reasonably constant within the focal volume (R. M. Williams and W. R. Zipfel, unpublished data; Richards and Wolf, 1959), so that to a first approximation the SHG polarization characteristics are not affected by the focus (Stoller et al., 2002b). By inspection of Eq. 3, a linearly polarized beam at an angle Φ with respect to the tendon produces an SHG intensity described by (Freund et al., 1986):

$$\begin{aligned} I_{\mathrm{y}}(\Phi) &= I_{\mathrm{p}}[\rho \cos^2 \Phi + \sin^2 \Phi]^2 \\ I_{\mathrm{x}}(\Phi) &= I_{\mathrm{p}}[\sin 2\Phi]^2, \end{aligned} \qquad (4)$$

where I_{p} is the total intensity measured with a perpendicularly polarized illumination beam and the ratio $\rho = (\beta_{\mathrm{yyy}}/\beta_{\mathrm{yxx}})$ is a measure of the fiber's axial polarizing effects. These equations were used to fit the output polarization of the SHG field.

Theory: SHG field propagation from a focused beam polarized parallel to the fibril axis

The local field distribution within the focus is extremely important for determining the propagation direction of the SHG field. For these experiments, the illumination beam was adjusted for linear polarization parallel to the fiber. The fibrils within the fiber are generally, but not entirely, aligned to the fiber axis. In the simplest case where the fibril is parallel to the fiber, collagen SHG is describable by a single hyperpolarizability element β_{yyy} giving emission also parallel to the fibril (Eq. 3). The electric field profile for a linearly polarized, + z-directed beam at the focus of an overfilled high-N.A. focus can be calculated exactly (Richards and Wolf, 1959), but for nonlinear applications is well approximated by a three-dimensional (3-D) Gaussian volume with a planar phase profile exhibiting a reduced axial wave vector ξk_ω (Moreaux et al., 2000):

$$\mathbf{E}_\omega(x,y,z) = -i\mathrm{E}_{\omega 0}\exp\left(-\frac{(x^2+y^2)}{w^2} - \frac{z^2}{w_z^2} + i\xi k_\omega z\right)\hat{\mathbf{y}}, \quad (5)$$

where ω is the angular frequency of the fundamental, $\hat{y}$ is the polarization direction, $k_\omega = 2\pi n_\omega/\lambda_\omega$ is the unfocused wave vector with a specimen index of n_ω, ξ is the wave vector reduction factor due to focusing that accounts for a reduction in axial momentum by conversion to lateral momentum components within the focus, and w and w_z are the 1/e radii of the focal ellipse in the lateral and axial directions, respectively. Fits to exact field calculations (Richards and Wolf, 1959) yield explicit values for the size of the focal volume (Zipfel et al., 2003b):

$$w = \frac{0.32\lambda_\omega}{n_\omega \sin\Theta} \quad \text{and} \quad w_z = \frac{0.53\lambda_\omega}{n_\omega(1-\cos\Theta)}, \quad (6)$$

where $n_\omega \sin\Theta$ is the N.A. of the microscope objective. For low N.A. (<0.8), ξ can be approximated by $\xi \approx \cos(\Theta/\sqrt{2})$ (Moreaux et al., 2000). Note that the Gouy phase anomaly (Born and Wolf, 1980) is distributed approximately linearly over the focal volume. For weak focusing $\Theta \to 0$, the phase shift over half the focal volume $k_\omega w_z - \xi k_\omega w_z \approx \pi/2$ as expected.

The second-harmonic field at any point (R, θ, φ) in the far field (Fig. 1) was calculated by summing contributions from all induced nonlinear dipole radiators within the focal volume (Moreaux et al., 2000; Mertz and Moreaux, 2001):

$$\begin{aligned}\mathbf{E}_{2\omega}(\theta,\varphi,R) &= \frac{\eta\beta_{yyy}}{R}\mathrm{E}_{\omega 0}^2 \sin\psi\hat{\boldsymbol{\psi}} \\ &\times \iiint dxdydz\, C(x,y,z)\exp\left(\frac{-2(x^2+y^2)}{w^2} - \frac{2z^2}{w_z^2}\right) \\ &\times \exp(-ik_{2\omega}(z\cos\theta + x\sin\varphi\sin\theta + y\cos\varphi\sin\theta)), \quad (7)\end{aligned}$$

where $\eta = \omega^2/\pi\varepsilon_0 c^2$, $C(x, y, z)$ is the spatially heterogeneous concentration of scatterer, $k_{2\omega} = 2\pi n_{2\omega}/\lambda_{2\omega}$ is the wave vector of the scattered emission, and ψ is the angle subtended from the y axis (the direction of the induced second-harmonic dipole) to the point of observation:

$$\sin\psi = (\sin^2\theta\cos^2\varphi + \cos^2\theta)^{1/2}. \quad (8)$$

The scatterer distributions $C(x, y, z)$ for the various calculations are described in the relevant figure captions. Calculations were made with array processing routines written in IDL (Research Systems, Boulder, CO). In all cases, the integration was carried out over a 3-D array at least five times larger than the focal volume using a voxel size $<(\lambda_\omega/20)^3$. Forward-propagating SHG (F) is the total $\mathbf{E}_{2\omega}^2$ produced for a fixed observation distance R with $-\pi/2 \le \theta \le \pi/2$ and the backward-propagating SHG (B) is the total $\mathbf{E}_{2\omega}^2$ with $\pi/2 \le \theta \le 3\pi/2$. Trial calculations performed using the exact field distribution (Richards and Wolf, 1959) yielded results consistent with the Gaussian approximation of the illumination field (Eq. 5). Note that these calculations describe the propagation of induced y-polarized SHG from a y-polarized fundamental on a y-aligned fibril. For a nonparallel fundamental, the induced second-harmonic dipole is generally nonparallel. Perpendicular field components are calculated similarly with a different β matrix element and a different ψ. They yield qualitatively similar F/B results in terms of scatterer distribution. These results are not presented within this article.

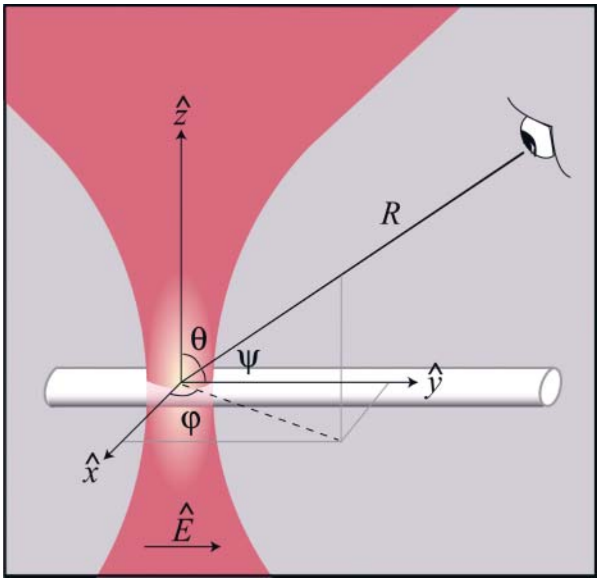

FIGURE 1 Diagram of coordinate system for calculating the SHG field at an observation point (R, θ, φ) from an arbitrary distribution of nonlinear scatterer within the focal volume. In this case, the nonlinear scatterer is distributed uniformly in a rod along the $\hat{y}$ axis. In all SHG field-propagation calculations, the illumination incidence is directed along the + $\hat{z}$ axis and the illumination polarization as well as induced nonlinear dipoles are assumed to be entirely $\hat{y}$-polarized.

RESULTS

SHG polarization from tendon

Although the collagen hyperpolarizability matrix has previously been examined at both macroscopic and microscopic scales (Roth and Freund, 1979; Freund et al., 1986; Stoller et al., 2002a), we are now able to revisit these measurements with individual fibril resolution. Following previous approaches, we assume cylindrical symmetry, with the caveat that the fibrillar ''crimping'', or the characteristic fibril waviness, could make this assumption suspect. We obtained tendon images using a linearly polarized fundamental and an SHG analyzer, both at varying angles to the fiber axis. For analysis, we identified (by eye) tendon regions in which fibrils possess an orientation that is parallel to the fiber axis (Fig. 2 *a*, *yellow mask*). In Fig. 2 *b*, the average SHG polarization intensity from this region is plotted with an illumination polarization at 0° (*red*), 30° (*black*), 60° (*green*), and 90°(*blue*) to the fiber axis (*arrows*). Fits are constructed using Eq. 4, in which there are two fitting parameters: *Ip*, which is normalized to 1 and ρ, which determines the relative magnitudes of the curves. For this specimen, fits revealed $\rho = 2.6 \pm 0.2$. Previously ρ had been measured to be 1.2–2.0 in adult tendons (Freund et al., 1986; Stoller et al., 2002a) and as little as 0.8 in immature tendons (Roth and Freund, 1979). However, those values were

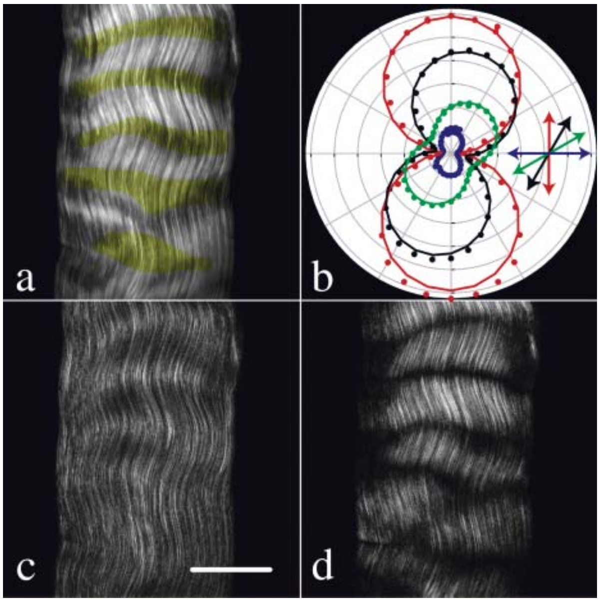

FIGURE 2 SHG polarization from individual fibers. (*a*) To determine the intrinsic fibril ρ, regions are selected in which fibrils are all oriented parallel to the fiber axis (*yellow mask*). (*b*) The SHG polarization intensity is measured from these regions by imaging with an analyzer placed between the specimen and the forward SHG detector. The curves displayed are from a linearly polarized fundamental at 0° (*red*), 30° (*black*), 60° (*green*), and 90° (*blue*) to the fiber axis (*colored arrows*). Note the differences in images acquired with an analyzer oriented parallel (*c*) and perpendicular (*d*) to the fiber axis. In this case, the SHG is induced with a fundamental that is polarized perpendicular to the fiber axis. Scale bar = 50 μm.

measured from whole fibers or from fiber regions without the ability for resolving individual fibrils. If we analyze regions where the fibrils are not aligned to the fiber axis, the goodness-of-fit to Eq. 4 is degraded and smaller ρ values result (data not shown). We note that our cylindrical symmetry assumption for the hyperpolarizability matrix is only truly valid at the individual fibril level and therefore fits to Eq. 4 are only expected for parallel fibrils. The combined effects of fibril directionality and illumination polarization have been described in detail elsewhere (Stoller et al., 2002b).

Taken together, these results suggest that the intrinsic single fibril polarizing effects are greater than previously estimated. Macroscopic measurements of ρ are significantly perturbed by fibrillar crimping (Stoller et al., 2002b), which is highly variable with tissue age, tissue type, or applied tension. Note that using an illumination polarization perpendicular to the fibril axis with simultaneous observation of parallel and perpendicular SHG emission (Fig. 2, *c* and *d*) results in images possessing a dramatic banding pattern, useful for analysis of crimp behavior. With perpendicular illumination polarization and a perpendicular SHG analyzer, signal from nonparallel fibrils is quite prominent whereas that from parallel fibrils is absent. For example, the green curve in Fig. 2 *b* represents the SHG intensity distribution from a fibril illuminated with a fundamental at 60° from the fibril (or perpendicular illumination on a fibril oriented at 30° to the fiber axis). A perpendicular analyzer would pick up signal at the 60° mark of this curve. The intensity at this point is roughly 10-fold that of the intensity from a parallel fibril with perpendicular illumination and a perpendicular analyzer (*blue curve*; 90° mark). To understand the propagation of SHG from a fibril-shaped distribution of scatterer, we analyze only the simplest case in which the fibrils are aligned parallel to the illumination polarization.

SHG emanates only from the fibril shell

A century ago, Gustav Mie discovered that objects extended along the optic axis ($\hat{z}$-direction) for a distance on the order of the emission wavelength exhibit linear scattering that is forward directed. This principle holds true for SHG (Mertz and Moreaux, 2001; Zipfel et al., 2003a) and other nonlinear processes (Volkmer et al., 2001; Cheng et al., 2002) as well. It results from the fact that extended scatterers emitting synchronously with a forward going fundamental generally remain phase matched only in the same forward-going direction. (Backward phase matching only occurs in the exceptional case when scatterers are distributed at a spatial frequency of $2/\lambda_{2\omega}$.) The phenomenon is somewhat complicated with the use of a highly focused illumination beam, but the general rule remains (Moreaux et al., 2000; Mertz and Moreaux, 2001; Volkmer et al., 2001).

In nonlinear microscopies, signal arises only from the scanned focal volume. Thus, for scatterers possessing a thickness comparable to the SHG wavelength, $\sim\lambda_{2\omega}$, the ratio of forward/backward signal (F/B) in SHG microscopy can be used to assess the axial size of the scatterer within the focal volume. This principle implied the ability to measure the thicknesses of fibrils within a laterally oriented tendon. Several comprehensive electron microscopy (EM) studies of fixed rat tail tendons have indicated that fibril diameters are $\sim\lambda_{2\omega}$ and consistently grow thicker with age (Parry et al., 1978; Craig and Parry, 1981). To make absolute F/B measurements from variously aged tendons (accounting for differences of optical transmissivity through the tendons) we normalized SHG F/B measurements to F/B measurements from fluorescent bead standards embedded within the tendon. Fig. 3, *a* and *b*, show typical images in the F and B directions, respectively.

A high-N.A. objective (e.g., 1.4 N.A. oil) typically possesses a working distance ($\sim$100 μm) inadequate for imaging tissue explants. Even tendon specimens, which are relatively thin (several hundred microns for an adult tendon) and clean, can only be imagined selectively with oil-immersion optics. Furthermore, to collect most of the forward-directed SHG, one must use a collection N.A. roughly equivalent to the illumination N.A. (Moreaux et al., 2000). The combination of high N.A. forward and backward collection limits the specimen thickness to ~100 μm. Thus, we used a high-N.A. objective only for selectively imaging fibrils where the highest resolution was required. We performed most calculations and experiments with a medium N.A. (0.75) to conform to general imaging conditions applicable to collagenous tissue explants. Note that the objective N.A. is not a big factor in F/B directionality of SHG propagation (calculations not shown). F/B depends primarily upon the axial extent of the scatterer as compared to the illumination wavelength.

Fig. 3, *a* and *b*, shows that the collagen fibrils are not significantly forward propagating as compared to the bead standards. If the collagen fibrils consisted of solid scatterer throughout, differently aged fibrils, with differing diameters (Parry et al., 1978; Craig and Parry, 1981), would be expected to exhibit F/B differences over orders of magnitude. The inserts in Fig. 3, *a* and *b*, contain images of beads interspersed among small glycine crystals. (Both glycine and hydroxyproline, two major constituents of collagen fibrils, generate second harmonic in crystal form.) By comparison the crystal rods are significantly forward propagating (F/B ~ 80). Fig. 3 *c* shows a plot of F/B calculated to emanate from varying diameter solid rods of scatterer (*solid line*; calculated via Eq. 7). Note that resonance effects occur at $\lambda_{2\omega}/2$ intervals, from increases in backward scattering at specific diameters. Fibril thicknesses within the same tendon are in fact known to vary over hundreds of nm (Parry et al., 1978) and would be expected to exhibit highly variable F/B values even within the same fiber. We were surprised to find that the measured F/B for tendon is close to one and remains relatively constant over all fibrils within a specimen and between all age specimens (Fig. 3 *c*, *circles*). These results are instead consistent with SHG emanating from a fibril modeled as a thin ($<\lambda_{2\omega}/20$) hollow tube (*dotted line*; calculated via Eq. 7). Note that the fibril age to diameter mapping was accomplished using published EM data from fixed tendons (Parry et al., 1978; Craig and Parry, 1981). Unfixed tendons are ~30% larger (Parry and Craig, 1977) and thus would be expected to exhibit even larger F/B increases with age if SHG signal emanated from the entire fibril volume, rather than from its shell.

When fibrils are large enough to be resolved with a high-N.A. objective, the SHG shell can be imaged directly. Fig. 3 *d* shows a projection of sequential lateral SHG images through laterally oriented fibrils and Fig. 3 *e* shows a single optical

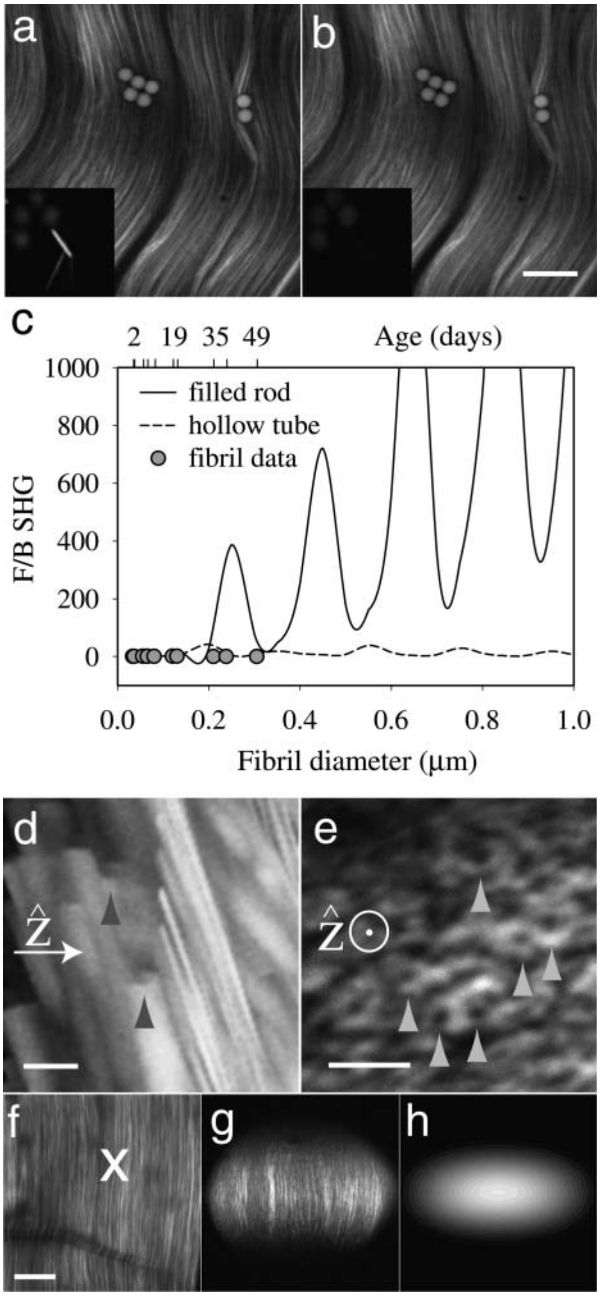

FIGURE 3 SHG emanates from the fibril shell only. (*a* and *b*) SHG from tendon is not significantly forward directed as shown by images of a 35-day tendon in the forward (*a*) and backward (*b*) directions. Absolute F/B is determined by normalization to F/B from 6-μm fluorescent beads, in which *F/B* ~ 1. Shown in the inserts are F and B images of beads as compared to small rod-shaped glycine crystals, which clearly exhibit forward scattering. (*c*) F/B data from tendon suggest that the collagen fibril possesses a scatterer distribution more like a hollow tube than a solid rod. F/B data from fibrils of varying ages (*circles*), and thus varying diameters, are consistent with calculations (Eq. 7) of F/B from a thin shell (with a thickness $< \lambda_{2\omega}/10$, *dashed line*) rather than a solid rod (*solid line*). Each circle represents measurements from at least three tendons; error bars are too small to be visualized on the scale of this graph. The curves were calculated for a fibril centered in the focal spot; however, decentering the fibril had no significant effects on the curves. (*d* and *e*) High-resolution images reveal the hollow-tube appearance of resolvable fibrils (at *arrowheads*). An oblique projection (*d*) and a lateral cross section (*e*) acquired from adult tendons with a Zeiss 40 × 1.4 N.A. oil objective. (*f–h*) The fibril diffraction pattern is consistent with SHG emanating from a hollow shell. To examine the SHG profile from a single fibril, a beam is focused at the indicated stationary location (*X* in *f*) in an adult tendon. The resulting diffraction pattern (*g*), imaged at the objective back aperture, matches that calculated for a thin hollow tube 0.25 μm in diameter (*h*). This experiment was carried out with a longer wavelength $\lambda_\omega = 880$ nm to ensure sensitivity of the camera to the SHG. The scale bars are 20, 2, 2, and 50 μm for *b*, *d*, *e*, and *f*, respectively.

section through axially oriented fibrils. The large resolvable fibrils (*arrowheads*) resemble hollow tubes rather than solid rods. In both cases, the apparent shell thickness of the tubes is measured to be at the resolution limit for the objective and wavelength used: 0.2–0.3 μm for a 1.3-N.A. objective at 780 nm. When the focal volume is smaller than the scattering volume (typical in microscopy), it is known that the SHG signal is greatly enhanced at the surface (Boyd, 1992). However, this surface enhancement with a focused beam only occurs from surfaces perpendicular to the optic axis and would not explain the appearance of the axially oriented surfaces evident in both figures. Furthermore, this surface-radiating property is not due to electric quadrupole and magnetic dipole effects producing surface enhancements in otherwise SHG-free centrosymmetric structures. Such effects result from symmetry breaking at the surface and are most pronounced with a fundamental that is perpendicularly polarized with respect to the surface (Heinz, 1991). With collagen, a highly noncentrosymmetric molecular assembly, SHG polarization is primarily parallel to the fibril surfaces and greatly enhanced with a parallel fundamental polarization (Fig. 2 *b*).

Taken together, the F/B ratio being of order unity, the hollow-tube images of large fibrils, and the polarization dependence of the radiating SHG, all suggest that SHG emanates only from the fibril shell rather than from its bulk as had previously been assumed by reference to EM micrographs of dried fibrils that appear somewhat uniform throughout (Parry and Craig, 1977). These diverse measurements suggest that the SHG shell is a physical characteristic of wet fibrils, not an optical effect.

A further check shows that a stationary beam at a single point in an adult tendon (Fig. 3 *f*, location *X*) produces an SHG intensity profile at the Fourier plane in the forward direction (Fig. 3 *g*) with an ellipticity consistent with that calculated (Eq. 7) for a thin hollow tube with a 0.2–0.3-μm diameter (Fig. 3 *h*, 0.25 μm diameter). This fit produces a reasonable estimate for an adult tendon fibril (Parry et al., 1978; Craig and Parry, 1981). Diffraction patterns from other fibrils are similar. The fringes in the imaged pattern (Fig. 3 *g*) are due to subsequent SHG scattering through the remainder of the tendon thickness, which was not accounted for in the calculations.

Low ionic strength results in a dramatic increase in F/B

Collagen SHG is expected to be extremely sensitive to the biochemical properties of the solution in which the fibrils reside. In the previous section we found the measured F/B to be relatively independent of fibril diameter. Additionally, we have found F/B to be insensitive to pH (in physiological ranges) and to osmotic stress—both from small and large osmolites (data not shown). However, F/B does change dramatically with solution ionic strength. Fig. 4, *a–d*, shows F and B images of a mature tendon at 2 and 200 mM NaCl concentrations, respectively. There are no resolvable morphological changes in the SHG images, even when examined at high resolution, but the magnitude of F/B is 10-fold higher under low-salt conditions.

Fig. 4 *e* shows a graph of F/B from fresh (*closed circles*) and paraformaldehyde-fixed (*open circles*) tendons at increasing salt concentrations. Decreasing F/B values with increasing ionic strength are not immediately reversible. Once a tendon has been immersed in a high-salt solution, a several-hour rinse is necessary to recover high F/B values. Paraformaldehyde fixing a tendon in water locks in the secondary and tertiary protein structure at low salt, resulting in a suppressed F/B decrease upon introduction of salt. These results imply that the F/B decrease with ionic strength is due to a subresolution structural change.

One explanation for a dramatic F/B decrease upon salt introduction would be a ‘‘thinning’’ of the shell from which the SHG emanates. For F/B to be sensitive to shell-thickness changes, the shell must be thick enough to sample differing illumination phases (at least $\sim\lambda_{\omega}/20$). Precise F/B values are dependent upon the width of the fibril, and its position and orientation within the illumination beam. Fig. 4 *f* shows a graph of calculated F/B values for laterally oriented tubes of differing diameters (numbers are in nm) as a function of shell thickness. Note that as expected F/B values are dependent on the exact size of the fibrils due to resonance effects in backward-propagating SHG, but there is a clear trend toward increasing F/B values with increasing shell thickness. Off-centering the fibril within the illumination beam changes the shape of the curve slightly (see the *solid* and *dotted lines* for the centered and off-centered 380-nm diameter fibril), but does not affect the overall conclusion. Using this graph, we estimate that a tendon in physiological saline ($F/B < 10$; Fig. 4 *e*) possesses a shell thickness $<$50 nm. For an average adult 380-nm diameter fibril (Parry et al., 1978), an $F/B \sim 80$ would imply a shell thickening to $>$100 nm while immersed in low salt. The insert figures show high-resolution images of fibrils from approximately the same position in an adult tendon immersed in 200 mM (panel *g*) and 2 mM NaCl (panel *h*). In this case, the forward and backward channels are both normalized to the same average value, the forward image is shown in green pseudocolor and the backward image is shown in red pseudocolor. Note that the fibrils in high salt (presumably thin shelled) show little variability in F/B (visualized as fibril color), whereas the fibrils in high salt (presumably thicker shelled) show significant variability. The graph (Fig. 4 *f*) predicts this effect for a collection of fibril diameters. Clearly the exact magnitude of the shell thickness change depends upon the fibril diameter distribution, which is unknown. However, the fact that dramatic F/B changes occur around physiological salt concentrations (Fig. 4 *e*), makes this measurement a potentially useful technique for assessing collagen hydration conditions.

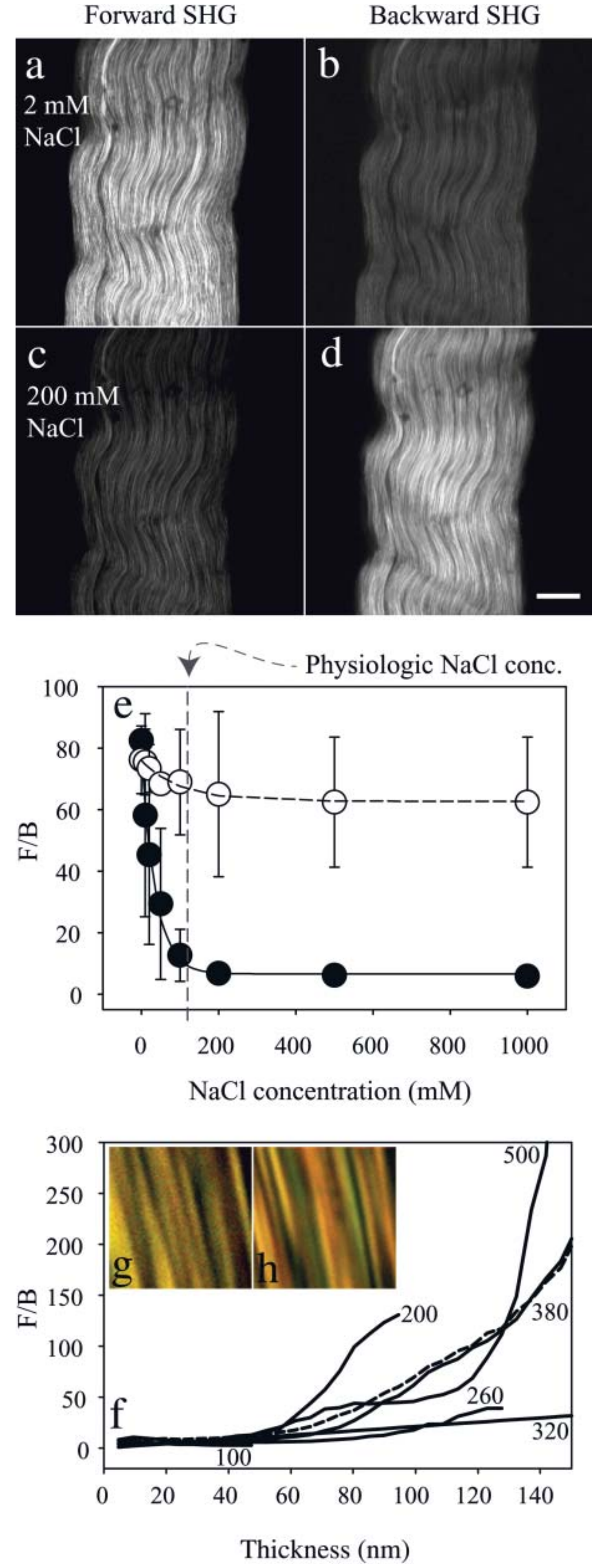

FIGURE 4 F/B values are dependent upon solution ionic strength as shown by the forward (*a* and *c*) and backward (*b* and *d*) images of an adult tendon at low (*a* and *b*) and high (*c* and *d*) NaCl concentrations. Scale bar = 50 μm. The dramatic decrease of F/B observed upon addition of salt (*e*; ●) is suppressed in tendons initially paraformaldehyde fixed in water (*e*; ○). (*f*) Calculated F/B values from various diameter tubes (numbers indicating diameters are in nm) show a clear increase with shell thickness. For the 380-nm tube, a calculation is made with the tube centered within the focal volume (*solid line*) as well as off-centered by the radius of the tube (*dotted line*). High F/B values from fibrils in pure water are consistent with a swelling of the shell from which the SHG emanates. The insert images show images of fibrils immersed in 200 mM (*g*) and 2 mM NaCl (*h*). In this case, images in the forward and backward directions are both normalized to the same average value, the forward image is shown in green pseudocolor and the backward image is shown in red. As predicted for a distribution of fibril diameters, the fibrils in low salt show significant F/B variability (visualized as color variability), whereas those in high salt do not.

Immature fibril segments are aligned and scatter prominently in the backward direction

Although the average F/B does not change by orders of magnitude with tendon maturation, it does exhibit subtle changes. For instance F/B for an infinitely thin fibril is calculated to be $F/B \sim 1$, whereas a 380-nm tube with infinitely thin walls should exhibit $F/B \sim 5$ (calculations not shown). Because tendons undergoing fibrillogenesis exhibit fibrils of all thicknesses, high-resolution images of young tendon appear strikingly different depending on the direction of SHG collection (Fig. 5, *a* (forward) and *b* (backward)). By contrast, images from the mature fibrils in adult tendon are identical in the F and B directions (Fig. 5, *c* and *d*, respectively). In immature tendon, backward SHG images exhibit a punctate distribution attributable to small-diameter, segmental collagen. Serial EM sections have shown that in two-week-old chicken tendon, most fibrils are <20 μm in length (Birk and Linsenmayer, 1994), with segment-segment fusion proceeding subsequently to form mature, continuous fibrils. Presumably the same process occurs in young rat tendon, but our images show that most segments are a few microns or less in length. We observe the same spotty pattern in young periosteum (data not shown). In both tendon and periosteum, these fibril segments are sometimes distributed nonuniformly along the collagen fibrils (Fig. 5 *b*), with a periodicity similar to that of the super fibrillar crimps.

The question then arises as to whether newly forming fibrils are less ordered than their adult counterparts. To address this question, we measured the polarization characteristics of the emitted backward SHG from fibril segments. Again mature fibrils are more prominent in the forward channel (Fig. 5 *e*), whereas immature fibril segments produce relatively more backward-directed SHG (Fig. 5 *f*). In this case the backward emission polarizations were separated and the resulting images color-coded (perpendicular to tendon, *purple*; parallel, *yellow*). The clear banding pattern of this representative image, reminiscent of that for a fully organized adult tendon (Fig. 2, *c* and *d*), shows that even the punctate fibril segments radiate SHG polarized according to the neighboring fibril directionality. Thus, they are well aligned even when they are in their immature segmental form. This finding corroborates theories of fibril segment

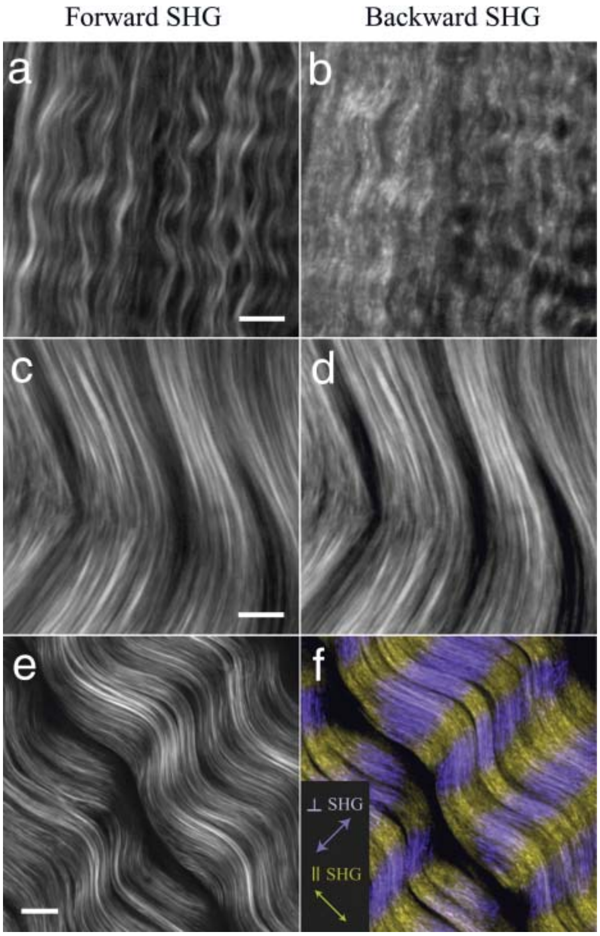

FIGURE 5 Immature fibril segments indicative of ongoing fibrillogenesis can be imaged in the backward direction. Fibril segments in a two-day tendon are more prominent in the backward image (*b*) than the forward image (*a*), whereas F and B images from mature tendon (*c* and *d*, respectively) are identical. (*e*) An image from a 19-day tendon collected in the forward direction shows mostly mature fibrils. (*f*) As indicated by their polarization, immature fibril segments are aligned to the fibril directionality. The backward-directed SHG is separated into two channels depending on the emission polarization (*purple* = perpendicular and *yellow* = parallel to the tendon axis as indicated by *colored arrows*). In the last case, the fundamental was polarized perpendicular to the tendon axis. All scale bars = 10 μm.

formation in which fibrils are produced in long and aligned compartments or channels within the fibroblasts that produce them (Trelstad and Hayashi, 1979; Birk and Linsenmayer, 1994). The smaller macroscopic ρ values measured in younger tendons (Roth and Freund, 1979) are thus likely to be due to the higher quantity of super fibrillar ''crimps'' than to a disorganization of the immature fibril segments.

DISCUSSION

A collagen fibril is described usually as a mass of microfibrils that aggregate laterally into a relatively homogeneous strand. By quantifying the relative amount of forward-to-backward propagating SHG, we have shown that SHG cannot emanate from the whole fibril volume in fibrils of wet tendon. Such a conclusion is drawn from the general rule that scatterers extended along the optic axis ($\lambda_{2\omega}$) are strongly forward scattering. Adult tendon fibrils are known to be of this thickness and yet when laterally oriented, they exhibit an F/B ratio close to unity. These and other results are consistent with the hypothesis that SHG emanates only from the fibril shell, a hypothesis that is extremely intriguing in light of recently acquired AFM images of collagen fibrils that exhibit kinks in bending patterns suggestive of hollow tubes rather than filled rods (Gutsmann et al., 2003). Furthermore, the thickness of the structural surface layer imaged with AFM (Gutsmann et al., 2003) is consistent with our estimated value ($<$50 nm). The sharpness of Bragg peaks from x-ray scattering analyses in wet rat-tail tendon have also indicated that the ordered regions may only be $\sim$30 nm across (Woodhead-Galloway, 1980), again consistent with our own estimation of the SHG shell thickness. Presumably this structural layer possesses the highest supermolecular order for generation of second harmonic. The chemical nature of the fibril interior has yet to be resolved, but we hypothesize that it is somewhat fluidic, relaxing to a centrosymmetric configuration. An F/B calculation for an adult fibril (0.38 μm diameter) reveals that β in the interior of the fibril must be $<1\%$ of that of the shell to exhibit fibril F/B values of order unity. A somewhat fluid interior would also corroborate other physical measurements in wet tendon specimens: the considerable degree of disorder evident from x-ray diffraction patterns (Hulmes et al., 1995) as well as the significant molecular mobility (around the fibril axis) evident from NMR relaxation times (Sarkar et al., 1983). Mobile water molecules are critical to both of these measurements.

High F/B values at low ionic strengths imply that the shell of the fibril swells under these conditions. Indeed it is known that immersing rat tendons in water results in a 10–20% increase in the average lateral spacing between collagen triple helices as assessed by x-ray scattering, along with an increase in water uptake and structural disorder (Svendsen and Koch, 1982; Leikin et al., 1994; Price et al., 1997). A swelling of the shell layer with the finding that the shell is the structural component of the fibril (Gutsmann et al., 2003) agree with empirically measured increases in stiffness with tendon hydration (Haut and Haut, 1997). With a cleverly designed endoscope, in which collagenous tissue is gently pulled between two optical fibers with a scattering standard, high F/B values could be used to diagnose abnormal hydration levels, such as those indicative of injury or various surgical procedures (Thornton et al., 2001). However, high F/B values could also reflect tissue positioning such that fibrils adopt a more axial alignment with respect to the optical fibers. Further nonimaging endoscopic potential resides in the ability to distinguish various collagen matrix types using a spectral ratio reporting the relative amounts of SHG/fluorescence. Although tendon collagen shows virtually no fluorescence (Zipfel et al., 2003a), dermal collagen shows quite a significant amount (data not shown), a fact that may relate to the amount of collagen glycosylation and cross-linking (Monnier et al., 1984).

Note that quantifying the angular distribution of coherent scattered light is a general method for determining the spatial frequencies of scattering objects. Using SHG microscopy enables these measurements to be performed at specific sites within optically thick specimens. Collagen fibrils are particularly amenable to such measurements because they are huge molecular assemblies, possessing widths comparable to optical wavelengths and nonlinear susceptibilities that are quite large. Using this method, we have demonstrated a physiologically relevant structural change in tendon fibrils of a size scale smaller than the resolution limit of the microscope. Although the collagen fibril offers a particularly clear application, this method is generalizable to any problem necessitating discrimination between axial object sizes in any coherent microscopy. For example SHG (~400 nm) from microtubules in laterally oriented neuronal axons are reported to have an $F/B \sim 10$ (Dombeck et al., 2003). Because these structures are known to have a diameter of only 30 nm ($<\lambda_{2\omega}/10$), the relatively high F/B can be interpreted to mean that the microtubules coherently add throughout the several hundred nanometer axon cross section. In other words, the induced dipoles from microtubues are aligned, a fact that is corroborated by polarization measurements in conjunction with EM studies of microtubule polarity (Baas et al., 1988). Another example stems from the ability of epi-collected CARS (as compared to forward-collected CARS) to discriminate signal of an axially finite source from the axially extended background (Cheng et al., 2002). Although knowledge of the scatterer shape as well as the directionality of the induced dipole is necessary for an exact calculation of coherent scattering propagation, it is the axial extent of the scatterer that ultimately determines F/B.

Because of the high organization of biological tissues, imaging will be essential for obtaining maximal potential from collagen endoscopy. The fact that immature fibrils can be distinguished from mature fibrils in the backward direction by resolving punctate structure from segmental collagen is extremely fortuitous because the penetration depth for tissue SHG microscopy is usually limited to several hundred microns. Clearly most imaging endoscopes designed for live animal and eventually human applications will rely exclusively on backward-scattered light. The ability to identify regions of active fibrillogenesis along with recent developments in the remote delivery of ultrafast pulses through microstructured optical fibers (Ouzounov et al., 2002) suggest that endoscopic collagen SHG microscopy may exhibit diagnostic potential for assaying collagen repair and regrowth after injury (Kobayashi et al., 1999) or for evaluating disease states such as malignancy progression. Increased synthesis and degradation of types I and III collagens are known to occur in the tissue surrounding cancerous lesions (for example, see Heino, 1996). Identification of immature segmental collagen in the backscattered direction may provide the impetus for a relatively noninvasive endoscopic tool for identifying tissue regions with high collagen turnover.

The authors thank Prof. Cornelia Farnum, Dan Dombeck, Dr. Peer Fischer, and Prof. Alexander Gaeta for illuminating discussions and help with this manuscript.

This research was supported by the National Institute for Biomedical Imaging and Bioengineering (grant No. 9 P41 EB001976-16) and the National Cancer Institute (grant No. R33 CA094311).

REFERENCES

Baas, P. W., J. S. Deitch, M. M. Black, and G. A. Banker. 1988. Polarity orientation of microtubules in hippocampal neurons: uniformity in the axon and nonuniformity in the dendrite. *Proc. Natl. Acad. Sci. USA.* 85:8335–8339.

Barad, Y., H. Eisenberg, M. Horowitz, and Y. Silberberg. 1997. Nonlinear scanning laser microscopy by third harmonic generation. *Appl. Phys. Lett.* 70:922–924.

Birk, D. E., and T. F. Linsenmayer. 1994. Collagen fibril assembly, deposition, and organization into tissue-specific matrices. *In* Extracellular Matrix Assembly and Structure. P. D. Yurchenco, D. E. Birk, and R. P. Mecham, editors. Academic Press, San Diego, CA. 91–128.

Born, M., and E. Wolf. 1980. Principles of Optics. Pergamon Press, New York, NY.

Boyd, R. W. 1992. Nonlinear Optics. Academic Press, Boston, MA.

Brown, E., T. McKee, E. DiTomaso, A. Pluen, B. Seed, Y. Boucher, and R. K. Jain. 2003. Dynamic imaging of collagen and its modulation in tumors in vivo using second-harmonic generation. *Nat. Med.* 9:796–800.

Campagnola, P. J., A. C. Millard, M. Terasaki, P. E. Hoppe, C. J. Malone, and W. A. Mohler. 2002. Three-dimensional high-resolution second harmonic generation imaging of endogenous structural proteins in biological tissues. *Biophys. J.* 82:493–508.

Cheng, J. X., A. Volkmer, and X. S. Xie. 2002. Theoretical and experimental characterization of coherent anti-Stokes Raman scattering microscopy. *J. Opt. Soc. Am. B. Opt. Phys.* 19:1363–1375.

Craig, A. S., and D. A. Parry. 1981. Growth and development of collagen fibrils in immature tissues from rat and sheep. *Proc. R. Soc. Lond. B Biol. Sci.* 212:85–92.

Denk, W., J. H. Strickler, and W. W. Webb. 1990. Two-photon laser scanning fluorescence microscopy. *Science.* 248:73–76.

Dombeck, D. A., K. A. Kasischke, H. D. Vishwasrao, M. Ingelsson, B. T. Hyman, and W. W. Webb. 2003. Uniform polarity microtubule assemblies imaged in native brain tissue by second-harmonic generation microscopy. *Proc. Natl. Acad. Sci. USA.* 100:7081–7086.

Fine, S., and W. P. Hansen. 1971. Optical second harmonic generation in biological systems. *Appl. Opt.* 10:2350–2353.

Flesken-Nikitin, A., R. M. Williams, W. R. Zipfel, W. W. Webb, and A. Y. Nikitin. 2004. Use of multiphoton imaging for studying cell migration in the mouse. *In* Cell Migration: Developmental Methods and Protocols, Vol. 294. G.-L. Guan, editor. Humana Press Totona, NJ. 335–345.

Freund, I., and M. Deutsch. 1986. Second-harmonic microscopy of biological tissue. *Opt. Lett.* 11:94–96.

Freund, I., M. Deutsch, and A. Sprecher. 1986. Connective tissue polarity. Optical second-harmonic microscopy, crossed-beam summation, and small-angle scattering in rat-tail tendon. *Biophys. J.* 50:693–712.

Guo, Y., H. E. Savage, F. Liu, S. P. Schantz, P. P. Ho, and R. R. Alfano. 1999. Subsurface tumor progression investigated by noninvasive optical second harmonic tomography. *Proc. Natl. Acad. Sci. USA.* 96:10854–10856.

Gutsmann, T., G. E. Fantner, M. Venturoni, A. Ekani-Nkodo, J. B. Thompson, J. H. Kindt, D. E. Morse, D. K. Fygenson, and P. K. Hansma. 2003. Evidence that collagen fibrils in tendons are inhomogeneously structured in a tubelike manner. *Biophys. J.* 84:2593–2598.

Haut, T. L., and R. C. Haut. 1997. The state of tissue hydration determines the strain-rate-sensitive stiffness of human patellar tendon. *J. Biomech.* 30:79–81.

Heino, J. 1996. Biology of tumor cell invasion: interplay of cell adhesion and matrix degradation. *Int. J. Cancer.* 65:717–722.

Heinz, T. F. 1991. Second-order nonlinear optical effects at surfaces and interfaces. *In* Nonlinear Surface Electromagnetic Phenomena. H-E. Ponath and G. I. Stegeman, editors. North-Holland, New York, NY. 353–416.

Hellwarth, R., and P. Christensen. 1974. Nonlinear optical microscopic examination of structure in polycrystalline ZnSe. *Opt. Commun.* 12:318–322.

Hulmes, D. J., T. J. Wess, D. J. Prockop, and P. Fratzl. 1995. Radial packing, order, and disorder in collagen fibrils. *Biophys. J.* 68:1661–1670.

Kobayashi, A., M. Sugisaka, K. Takehana, M. Yamaguchi, Eerdunchaolu, E. K. Iwasa, and M. Abe. 1999. Morphological and histochemical analysis of a case of superficial digital flexor tendon injury in the horse. *J. Comp. Pathol.* 120:403–414.

Larson, D. R., W. R. Zipfel, R. M. Williams, S. W. Clark, M. P. Bruchez, F. W. Wise, and W. W. Webb. 2003. Water-soluble quantum dots for multiphoton fluorescence imaging in vivo. *Science.* 300:1434–1436.

Leikin, S., D. C. Rau, and V. A. Parsegian. 1994. Direct measurement of forces between self-assembled proteins: temperature-dependent exponential forces between collagen triple helices. *Proc. Natl. Acad. Sci. USA.* 91:276–280.

Mertz, J., and L. Moreaux. 2001. Second-harmonic generation by focused excitation of inhomogeneously distributed scatterers. *Opt. Commun.* 196:325–330.

Monnier, V. M., R. R. Kohn, and A. Cerami. 1984. Accelerated age-related browning of human collagen in diabetes mellitus. *Proc. Natl. Acad. Sci. USA.* 81:583–587.

Moreaux, L., O. Sandre, and J. Mertz. 2000. Membrane imaging by second-harmonic generation microscopy. *J. Opt. Soc. Am. B.* 17:1685–1694.

Muller, M., J. Squier, K. R. Wilson, and G. J. Brakenhoff. 1998. 3D microscopy of transparent objects using third-harmonic generation. *J. Microsc.* 191:266–274.

Ouzounov, D. G., K. D. Moll, M. A. Foster, W. R. Zipfel, W. W. Webb, and A. L. Gaeta. 2002. Delivery of nanojoule femtosecond pulses through large-core microstructured fibers. *Opt. Lett.* 27:1513–1515.

Parry, D. A., G. R. Barnes, and A. S. Craig. 1978. A comparison of the size distribution of collagen fibrils in connective tissues as a function of age and a possible relation between fibril size distribution and mechanical properties. *Proc. R. Soc. Lond. B Biol. Sci.* 203:305–321.

Parry, D. A., and A. S. Craig. 1977. Quantitative electron microscope observations of the collagen fibrils in rat-tail tendon. *Biopolymers.* 16:1015–1031.

Price, R. I., S. Lees, and D. A. Kirschner. 1997. X-ray diffraction analysis of tendon collagen at ambient and cryogenic temperatures: role of hydration. *Int. J. Biol. Macromol.* 20:23–33.

Richards, B., and E. Wolf. 1959. Electromagnetic diffraction in optical systems.2. Structure of the image field in an aplanatic system. *Proc. R. Soc. Lond. A. Math. Phys. Sci.* 253:358–379.

Roth, S., and I. Freund. 1979. Second harmonic-generation in collagen. *J. Chem. Phys.* 70:1637–1643.

Roth, S., and I. Freund. 1981. Optical second-harmonic scattering in rat-tail tendon. *Biopolymers.* 20:1271–1290.

Sarkar, S. K., C. E. Sullivan, and D. A. Torchia. 1983. Solid state 13C NMR study of collagen molecular dynamics in hard and soft tissues. *J. Biol. Chem.* 258:9762–9767.

Stoller, P., B. M. Kim, A. M. Rubenchik, K. M. Reiser, and L. B. Da Silva. 2002a. Polarization-dependent optical second-harmonic imaging of a rat-tail tendon. *J. Biomed. Opt.* 7:205–214.

Stoller, P., K. M. Reiser, P. M. Celliers, and A. M. Rubenchik. 2002b. Polarization-modulated second harmonic generation in collagen. *Biophys. J.* 82:3330–3342.

Svendsen, K. H., and M. H. Koch. 1982. X-ray diffraction evidence of collagen molecular packing and cross-linking in fibrils of rat tendon observed by synchrotron radiation. *EMBO J.* 1:669–674.

Thornton, G. M., N. G. Shrive, and C. B. Frank. 2001. Altering ligament water content affects ligament pre-stress and creep behaviour. *J. Orthop. Res.* 19:845–851.

Trelstad, R. L., and K. Hayashi. 1979. Tendon collagen fibrillogenesis: intracellular subassemblies and cell surface changes associated with fibril growth. *Dev. Biol.* 71:228–242.

Volkmer, A., J. X. Cheng, and X. S. Xie. 2001. Vibrational imaging with high sensitivity via epidetected coherent anti-Stokes Raman scattering microscopy. *Phys. Rev. Lett.* 8702:023901.

Wang, W., J. B. Wyckoff, V. C. Frohlich, Y. Oleynikov, S. Huttelmaier, J. Zavadil, L. Cermak, E. P. Bottinger, R. H. Singer, J. G. White, J. E. Segall, and J. S. Condeelis. 2002. Single cell behavior in metastatic primary mammary tumors correlated with gene expression patterns revealed by molecular profiling. *Cancer Res.* 62:6278–6288.

Willetts, A., J. E. Rice, D. M. Burland, and D. P. Shelton. 1992. Problems in the comparison of theoretical and experimental hyperpolarizabilities. *J. Chem. Phys.* 97:7590–7599.

Williams, R. M., J. B. Shear, W. R. Zipfel, S. Maiti, and W. W. Webb. 1999. Mucosal mast cell secretion processes imaged using three-photon microscopy of 5-hydroxytryptamine autofluorescence. *Biophys. J.* 76:1835–1846.

Williams, R. M., W. R. Zipfel, and W. W. Webb. 2001. Multiphoton microscopy in biological research. *Curr. Opin. Chem. Biol.* 5:603–608.

Woodhead-Galloway, J. 1980. Structure of the collagen fibril: some variations on a theme of tetragonally packed dimers. *Proc. R. Soc. Lond. B. Biol. Sci.* 209:275–297.

Zipfel, W. R., R. M. Williams, R. Christie, A. Y. Nikitin, B. T. Hyman, and W. W. Webb. 2003a. Live tissue intrinsic emission microscopy using multiphoton excited intrinsic fluorescence and second harmonic generation. *Proc. Natl. Acad. Sci. USA.* 100:7075–7080.

Zipfel, W. R., R. M. Williams, and W. W. Webb. 2003b. Nonlinear magic: multiphoton microscopy in the biosciences. *Nat. Biotechnol.* 21:1369–1377.